IPSJ Transactions on Computer Vision and Applications Vol. 3 32–43 (June 2011)

Research Paper

Blind Deconvolution for a Curved Motion Based on Cepstral Analysis

Yuji Oyamada,[†1] Haruka Asai[†1,*1] and Hideo Saito[†1]

When a camera moves during its exposure time, the captured image is degraded by the motion. Despite the several decades of researches, image deconvolution to restore a blurred image still remains an issue, particularly in blind deconvolution cases in which the actual shape of the blur is unknown. The cepstral approaches have been used to estimate a linear motion. In this paper, we propose a Point Spread Function (PSF) estimation method from a single blurred image. We extend the classical cepstral approaches that have been used for Uniform Linear motion PSF estimation. Focusing on Uniform Non-Linear motion (UNLM) that goes one direction and potentially weakly curves, we solve the PSF estimation problem as a camera path estimation problem. To solve the ill-posed problem, we derive a constraint on the behavior of the cepstra of UNLM PSFs. In a first step, we estimate several PSF candidates from the cepstrum of a blurred image. Then, we select the best PSF candidate by evaluating the candidates based on the ringing artifacts on the restored images obtained using the candidates. The performance of the proposed method is verified using both synthetic images and real images.

1. Introduction

Camera motion during exposure time blurs the captured image. A blurred image g can be represented by a convolution of a latent image f and a function h as

$$g = f \otimes h, \tag{1}$$

where $\otimes$ denotes a convolution operator. Since the function h represents how a point light source is observed in a blurred image, it is called Point Spread Function (PSF).

Image deblurring, recovering a latent image given a blurred image, is called deconvolution because it is an inverse operation of convolution. Especially, when h is unknown, the problem is called blind deconvolution [17]. Since the problem is an ill-posed problem, there is infinite set of pairs of (f, h) that satisfies Eq. (1).

To solve the ill-posed problem, additional assumptions on f or h are required. A classical assumption for solving the ill-posed problem is constraints on camera motion. A uniform linear motion (ULM) can be represented by two parameters, motion direction and length. Thus, PSF estimation problem can be solved as parameters estimation problem. Since the features of ULM PSF is obviously observed in spectrum/cepstrum domain not image domain, there exist several approaches estimating a ULM PSF from spectrum [5),6),12),13),22),25),29),32)] or cepstrum [3),16),24),26),31)] of a blurred image. Ding, et al. analyzes the spectral behavior of parametric motions including uniform linear motion, accelerated linear motion, and linear harmonic motion [10]. Introducing a flutter shutter camera, they estimate the PSF by analyzing image power spectrum statistics. Another type of assumption is constraint on target scenes captured in the blurred image. This assumes that target scene consists of two regions, fore-ground and background. For such scene, motion blur smears alpha matte of the scene originally should be binary. Using this constraint, an energy function minimization finds a PSF well-representing the relation between multi-valued alpha matte of a blurred image and corresponding binary one of an unknown latent image [1),7),8),14),28)]. Recently, methods that constrain unknown latent images based on the natural image statistics have got attention to estimate a non-uniform and non-linear motion (NUNLM). The methods put assumption on histogram of a gradient image [11),18),27)] and motion blur effect on edges of latent images [15] and solve the problem by following Bayesian inference manner.

Each of these constraints has both merits and demerits. Constraint on PSF can provides analytical solution for the deconvolution problem, thus it should provide stable results. However, it strongly limits the target camera motion because of its parametric model. Constraint on scene relaxes the constraint on PSF shape. Energy minimizations on alpha matte allow us to deal with affine motion including rotation. However, target scene is limited and manual operations such as matting are required. In terms of complexity of PSF shape, constraint on unknown latent images is the best. However, Bayesian inference

†1 Graduate School of Science and Technology, Keio University
*1 Presently with Sony Corporation

severely required that blurred images follow the natural image statistics and there are many parameters to tune carefully.

1.1 Overview of Proposed Method

In this paper, we propose to relax the limitation of the traditional cepstral analysis based PSF estimation methods that have been used for ULM PSF estimation. Specifically, we propose a single image blind deconvolution for uniform non-linear motion that goes one direction and potentially weakly curves. Since we limit target camera motion as uniform motion, PSF estimation problem can be done by the camera path estimation problem. Preliminary results of this work were presented by Asai, et al. [2]. The main contributions of this paper are: Analyzing the cepstral behavior of both ULM and UNLM PSFs and propose a path integral based PSF estimation method; Evaluating the performance of both sub-processes and entire process of the proposed method; Investigating the performance of the proposed method for PSFs not supposed by our assumption, i.e., non-uniform motion and heavy curved motion; Demonstrating the results of various real world scenes to validate the effectiveness of the proposed method.

We first overview the classical cepstral approaches both theory and the ULM PSF estimation method in Section 2. Next, Section 3 clarifies the features of the cepstrum of blurred image degraded by UNLM and then propose a UNLM PSF estimation method based on the features. To evaluate the effectiveness of our method, we show the experimental result by using both synthesized data and real-world scenes in Section 4. Finally, Section 5 summarizes the contents of the paper.

2. Cepstral Analysis

In this section, we describe the behavior of the cepstrum of blurred images degraded by a ULM PSF.

2.1 Cepstrum

The cepstrum of an image is the inverse Fourier transform of the log power spectrum of the image as

$$\mathcal{C}(\text{image}) = \mathcal{F}^{-1}\left(\log\left|\mathcal{F}\left(\text{image}\right)\right|\right), \tag{2}$$

where $\mathcal{C}$ and $\mathcal{F}$ denote the cepstrum transform and the Fourier transform respectively. Since the cepstrum is the log power spectrum of a spectrum, cepstra have same features as spectra, e.g. a cepstrum has a positive peak at the center and is symmetrical about the peak. The important property of the cepstrum for image deconvolution is that the convolution of two images can be represented by the addition of their cepstra. Therefore the cepstrum of a blurred image C_g is represented by the addition of the cepstrum of a latent image C_f and one of a PSF C_h as

$$\begin{aligned} C_g &= \mathcal{C}(g) \\ &= \mathcal{F}^{-1}\left(\log\left|\mathcal{F}(g)\right|\right) \\ &= \mathcal{F}^{-1}\left(\log\left|\mathcal{F}\left(f \otimes h\right)\right|\right) \\ &= C_f + C_h. \end{aligned} \tag{3}$$

Note that C_h has much bigger values than C_f which means that C_h dominates C_g. Since the distribution of spectrum of PSF is relatively smaller than that of a latent image, C_h converges on the positive peak while C_f is distributed from low quefrency to high quefrency. Therefore, C_g can be considered as approximated C_h around the positive peak.

2.2 Cepstrum of a Blurred Image Degraded by ULM PSF

A ULM PSF is parameterized by two parameters, motion length L and motion direction θ. Rom [26] noted that the cepstrum of a ULM PSF has strong values along the motion direction θ and has periodic negative valleys of period L along the direction. **Figure 1** compares the cepstrum of a ULM PSF C_h and that of the blurred image C_g. Red pixels in the right figures show that C_h has periodic negative valleys along the motion direction while C_g has additional negative valleys around the positive peak. These additional valleys in C_g is derived from C_f. Blue pixels in the right figures show that C_h has strong values along the motion direction while C_g has additional horizontal and vertical lines. These lines are caused by an assumption on periodicity of images.

Prior works use these cepstral features to estimate a ULM PSF. One method simultaneously estimate blur motion θ and blur length L by finding a periodic negative valley nearest to the positive peak in the cepstrum of a blurred image C_g [16),31)]. However, when the latent image component C_f severely smears the periodic negative valleys, the simultaneous estimation mis-detects another negative valley that derived from C_f. For more stable detection, Moghaddam and Jamzad [24] eliminates potential directions that don't have strong values to

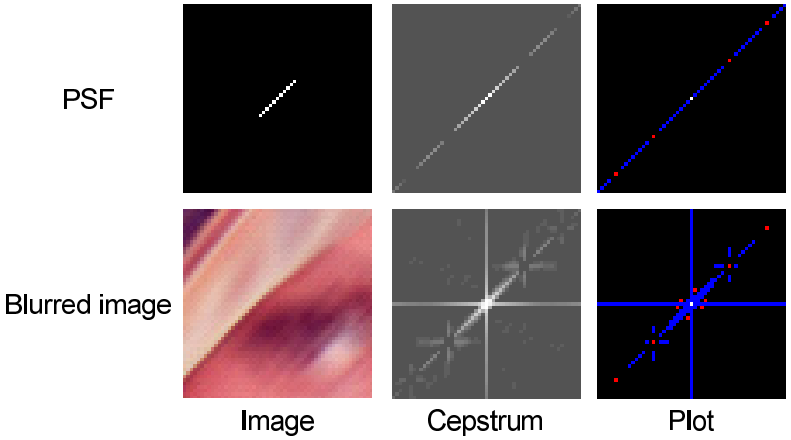

Fig. 1 Comparison of the cepstrum of a ULM PSF (top) and one of the blurred image (bottom). From left to right, image, cepstrum, and plotted values are shown. In the right figure, the positive peak of ceptrum, negative valleys, and strong values are plotted as white, red, and blue pixels respectively.

prevent such mis-detection. The method first estimates θ by finding a line that has strong values. Then, blur length L is estimated by finding a negative valley along the estimated direction θ. By separating the process, the method can stably estimate the parameters.

We consider such sequential ULM PSF estimation method [24] from another aspect. Suppose we detect several negative valleys from C_g and check lines each of which connects the positive peak and one of the negative valleys. A detected valley on a line that has strong values should be equivalent to one of the periodic valleys. Thus, the ULM PSF can be estimated by finding a line that maximizes the path integral between the positive peak and a negative valley. This path integral based PSF estimation can be formulated as

$$\hat{\mathrm{L}} = \arg\max_{\mathrm{L}} \int_{\mathrm{L}} C_g(p,q)ds, \tag{4}$$

$$\hat{h}(x,y) = \begin{cases} 1 & (x,y) \in \hat{\mathrm{L}} \\ 0 & \text{otherwise} \end{cases},$$

where L denote a set of lines, each of which connects the positive peak and one of negative valleys and ds denotes an elementary arc length of lines. The estimated line $\hat{\mathrm{L}}$ has same shape as the PSF and also the position of the corresponding valley tells us the parameters of the ULM PSF.

3. Our Approach

This section proposes a UNLM PSF estimation method based on cepstral analysis. First of all, we analyze the behavior of the cepstrum of a blurred image degraded by UNLM PSF in Section 3.1. Next, Section 3.2 re-formulates path integral based PSF estimation Eq. (4) to deal with a UNLM PSF, and then Section 3.3 describes the solution method.

As an input, our method takes a single blurred image obtained by a normal camera. We put some assumptions on a camera motion: the motion is uniform on a blurred image, a PSF for a blurred image; the motion is one-way, meaning a unidirectional PSF; the motion is under constant speed, meaning a binary PSF.

3.1 Cepstrum of a Blurred Image Degraded by UNLM PSF

Here, we analyze the behavior of the cepstrum of a UNLM PSF. Experience shows that the cepstrum of a UNLM PSF has strong values along the blur direction and that the cepstrum has distributed negative valleys along the motion direction. **Figure 2** compares the cepstrum of a UNLM PSF C_h and that of the blurred image C_g. Red pixels in the right figures show that C_h has negative valleys along the motion direction but they are not periodic. Same as a ULM PSF, C_g has additional negative valleys around the positive peak. Blue pixels in the right figures show that C_h has strong values along the motion direction. Different from a ULM PSF, the strong values are distributed not located on a line.

3.2 UNLM PSF Estimation Based on Cepstral Analysis

From the discussion above, we derive an assumption that the cepstrum of a UNLM PSF has unclear PSF shape that lies between the positive peak and one of negative valleys. In this section, we re-formulate the path integral based PSF estimation Eq. (4) based on the assumption. Basic strategy is same as ULM PSFs described above. We find a curve, not a line, that maximizes the path integral between the positive peak and a negative valley. The difference between ULM PSFs and UNLM PSFs is the way of comparison of path integral. In the case

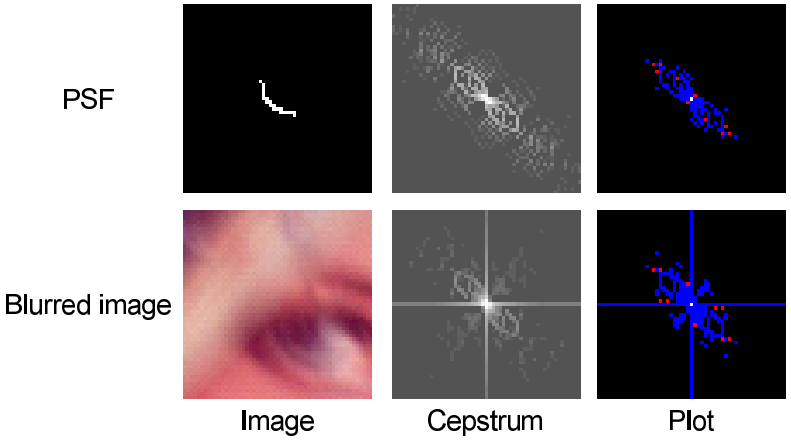

Fig. 2 Comparison of the cepstrum of a UNLM PSF (top) and one of the blurred image (bottom). From left to right, image, cepstrum, and plotted values are shown. In the right figure, the positive peak of ceptrum, negative valleys, and strong values are plotted as white, red, and blue pixels respectively.

of ULM PSF, Eq. (4) compares the values of path integral of detected negative valleys. However, such direct comparison can not be applied to the UNLM PSF because the strong values on C_g are not exactly on the PSF shape as shown in Fig. 2. Thus, the equation does not guarantee that the estimated path is equivalent to the PSF shape. Alternatively, we separate the problem into two sub-problems. Given N negative valleys of C_g, we first estimate paths as PSF candidates, and then choose the most likely candidate as final estimate.

The path integral equation Eq. (4) is re-formulated for UNLM PSFs as

$$\hat{\mathrm{C}}_i = \arg\max_{\mathrm{C}_i} \int_{\mathrm{C}_i} C_g(p,q)ds, \tag{5}$$

$$\hat{h}_i^{\mathrm{int}}(x,y) = \begin{cases} 1 & (x,y) \in \hat{\mathrm{C}}_i \\ 0 & \text{otherwise} \end{cases},$$

where C_i denotes a curve connecting the positive peak and one of the negative valleys R_i. Since a cepstrum is symmetric about the positive peak, the symmetric shape of an estimated path may be another candidate of the correct PSF. Thus, we regard both N estimated paths $\hat{h}^{\mathrm{int}}$ and their symmetric paths $\hat{h}^{\mathrm{sym}}$ as PSF candidates. Totally, we obtain $2N$ PSF candidates $\hat{h}^{\mathrm{can}} = \{\hat{h}_j^{\mathrm{can}} \mid j = 1, \ldots, 2N\}$ from N negative valleys.

Then, we estimate a PSF among the estimated candidates. The most likely PSF should satisfy the imaging equation Eq. (1). Thus, our method evaluates the candidates as

$$\hat{h} = \arg\min_{\hat{h}_j^{\mathrm{can}}} \left| g - f \otimes \hat{h}_j^{\mathrm{can}} \right|. \tag{6}$$

By separating the problem into sub-problems, we finally obtain the most likely PSF $\hat{h}$.

3.3 Implementation

This section describes the implementation of the proposed method: make the cepstrum of a blurred image more tractable; the detail of the path integral based PSF estimation of Eq. (5); the detail of the PSF candidates evaluation of Eq. (6).

C_f component reduction

The proposed PSF estimation algorithm tries to find a hidden PSF shape in the cepstrum of a blurred image C_g. For this purpose, the latent image component C_f is obstacle. To make C_h more clear, we reduce C_f by following the traditional works [16),20)]. We take an average of cepstra of partitioned blurred image g_k as

$$\overline{C}_g = \frac{1}{K}\sum_{k=1}^{K} C_{g_k} = \frac{1}{K}\sum_{k=1}^{K}(C_{f_k} + C_{h_k}) = (\overline{C}_f + \overline{C}_h) \approx C_h, \tag{7}$$

where K denotes the number of partition. As previously mentioned, we assume uniform PSF on a blurred image while f varies by region. In this case, C_{f_k} differs according to region while C_{h_k} is constant. Thus, averaging of Eq. (7) reduces the contribution of C_f while keeps C_h. PSF shape estimation algorithm uses $\overline{C}_g$ as an input.

Path integral based PSF shape estimation

Here, we describe the detail of PSF shape estimation Eq. (5). Since we assume a unidirectional camera motion, PSF should be a one-way path connecting the positive peak R_0 and a negative valley R_i. Thus, solving Eq. (5) is equivalent to finding a path maximizing path integral along a one-way curve. We regard this

problem as a kind of shortest path searching problem. Thus, we solve the problem by dynamic programming. Specifically, we apply the Dijkstra's algorithm [9]. Given an average cepstrum $\overline{C}_g$, we assign the value of $\overline{C}_g$ as a graph where each position $r_k = (p_k, q_k)$ corresponds to a node. An edge is defined to connect 3 neighboring nodes $r_{k+\Delta k} \in \{(p_k, q_k+1), (p_k+1, q_k), (p_k+1, q_k+1)\}$ given the positions of the negative valley $R_i = (P_i, Q_i)$ and the positive peak $R_0 = (0, 0)$ as

$$\mathrm{cost}\left(r_{k+\Delta k}\right) = \frac{\langle \overrightarrow{R_0 r_{k+\Delta k}}, \overrightarrow{R_0 R_i} \rangle}{\|\overrightarrow{R_0 r_{k+\Delta k}}\| \cdot \|\overrightarrow{R_0 R_i}\|}. \tag{8}$$

The cost function represents the cosine of the angle formed by R_i, R_0, and $r_{k+\Delta k}$. Since the cost function enforces a path to connect the peak and the valley with shorter length, the estimated path tends to be a smooth curve rather than a zigzag line. After taking integral from R_i to R_0, we find a path maximizing the path integral between the positive peak and the negative valley.

PSF candidates evaluation

Here, we describe the detail of PSF candidates evaluation. Equation (6) theoretically chooses the best PSF among PSF candidates but in practice it does not work because Eq. (6) uses unknown latent image f. Instead of f, we use a recovered image $\hat{f}_j$, deconvolution of $\hat{h}_j^{\mathrm{can}}$, for the evaluation as

$$\hat{h} = \arg\min_{\hat{h}_j^{\mathrm{can}}} \left| g - \hat{f}_j \otimes \hat{h}_j^{\mathrm{can}} \right|. \tag{9}$$

One may consider that Eq. (9) can not evaluate the PSF candidates because the term $\hat{f}_j \otimes \hat{h}_j^{\mathrm{can}}$ is theoretically same as g. However, the ringing artifacts caused by deconvolution algorithms make the term different from g in practice except when $\hat{h}_j^{\mathrm{can}}$ is a delta function. When a deconvolution algorithm uses wrong PSF, ringing artifacts appear. Even if a deconvolution algorithm uses the correct PSF, the ill-posedness of deconvolution increases ringing artifacts in proportion to the PSF size. Thus, we design an evaluation function that mainly evaluates the ringing artifacts derived from PSF mis-estimation and regularizes by the PSF size as

$$\hat{h} = \arg\max_{\hat{h}_j^{\mathrm{can}}} \left(\mathrm{Shape}\left(\hat{h}_j^{\mathrm{can}}\right) + \lambda \mathrm{Size}\left(\hat{h}_j^{\mathrm{can}}\right) \right), \tag{10}$$

$$\mathrm{Shape}\left(\hat{h}_j^{\mathrm{can}}\right) = \mathrm{NCC}\left(g, \hat{f}_j \otimes \hat{h}_j^{\mathrm{can}}\right),$$

$$\mathrm{Size}\left(\hat{h}_j^{\mathrm{can}}\right) = \frac{\mathrm{Width}^2\left(\hat{h}_j^{\mathrm{can}}\right) + \mathrm{Height}^2\left(\hat{h}_j^{\mathrm{can}}\right)}{\left\|\hat{h}_j^{\mathrm{can}}\right\|_0},$$

where $\|\cdot\|_0$ denotes L0 norm. Division by the L0 norm makes the evaluation function to favor a smooth curve over a zigzag line. The error term Shape() evaluates PSF candidates based on Eq. (9) and the regularization term Size() considers the PSF candidate's size.

To well-evaluate the PSF candidates, we should use an optimum deconvolution algorithm to compute $\hat{f}_j$. From the description above, we understand Eq. (10) evaluates the ringing artifacts caused by deconvolution algorithm while Eq. (6) evaluates how the PSF candidate satisfies the imaging equation. In this sense, the deconvolution algorithm should provide ringing artifacts according to PSF mis-estimation. This implicitly rejects state-of-the art deconvolution algorithms that usually include deringing process. Thus, we use Wiener filtering [30] to compute $\hat{f}_j$.

4. Experimental Results

This section validates the proposed method by using both synthesized images and real world images. Synthesized images are used to evaluate the performance of both each process and entire process of the proposed method. Then, we apply the proposed method to real world images. We further show the comparisons with other blind deconvolution methods. Through the experiments, the number of image partition K of Eq. (7) is set to 4 and the number of detected negative valleys N is set to 10.

4.1 Synthetic Experiments

In these synthetic experiments, we use 200 images from Berkley Segmentation Dataset as latent images and randomly generated PSFs to synthesize blurred images. We first assess sub processes of the proposed method, which are PSF shape estimation process and PSF candidates evaluation process. Next, we eval-

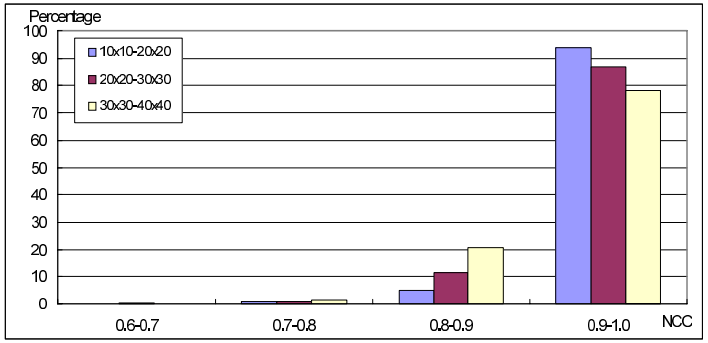

Fig. 3 Experimental result: NCC histogram of the restored images $\hat{f}$ and $\hat{f}_{\mathrm{best}}$ w.r.t. PSF size.

uate the entire proposed method by applying to synthesized images. Finally, we show the behavior of the proposed method for motion blurs which do not satisfy our assumption. Since the synthesized images are noise-free, we use Wiener filtering [30] as a deconvolution algorithm. To evaluate the estimated PSFs, we compare a restored image using estimated PSF with a restored image using the ground truth PSF not with the latent image because deconvolution algorithms can not perfectly recover the latent image even with the ground truth PSF.

PSF shape estimation process

We first evaluate the PSF shape estimation process. In Section 3.2, we derived an assumption that the cepstrum of a UNLM PSF has unclear PSF shape that lies between the positive peak and one of negative valleys. To validate the assumption, we input a correct negative valley, corresponding to a ground truth PSF, to Eq. (5) so that the process can ideally estimate the correct PSF. Since it is not easy to evaluate an estimated PSF by its shape, we compare the restored image obtained by the estimated PSF $\hat{f}$ with that by ground truth $\hat{f}_{\mathrm{best}}$. **Figure 3** shows the histogram of NCC of the restored images $\hat{f}$ and $\hat{f}_{\mathrm{best}}$ w.r.t. PSF size. It is natural that the process recovers higher NCC images for smaller size of PSFs. Empirically, NCCs below 0.9 are visually unacceptable. With this threshold, more than 70 percent of the trials are successful for all the sizes of PSFs. **Figure 4** shows some of the restored images. From left to right, the size of ground truth PSF is increasing. Red framed figures in $\hat{f}$ show the estimated

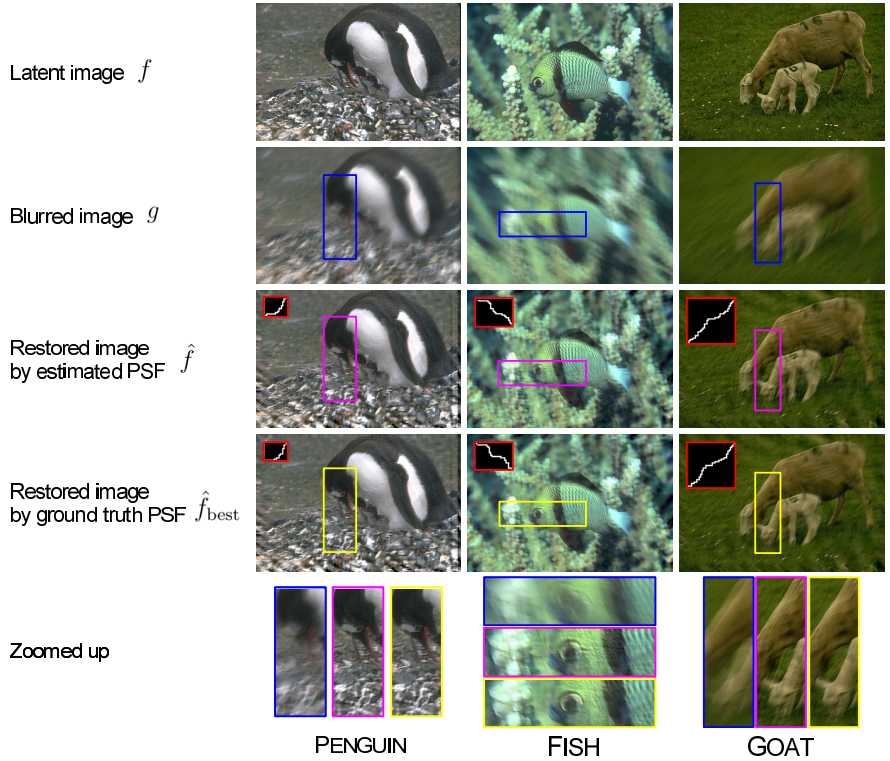

Fig. 4 Examples of the PSF shape estimation experiment. From top to bottom, latent images, blurred images, restored images by estimated PSFs, restored images by ground truth PSFs, and zoomed up of the restored images are shown. Red framed figures in restored images are PSFs used for deconvolution (for better visualization, we enlarge the PSFs 3 times the normal size). From left to right, PSF size is increasing.

PSFs while that in $\hat{f}_{\mathrm{best}}$ show the ground true PSFs. In both PENGUIN and FISH cases, PSF is well-estimated, thus the restored images by estimated PSF recover the detail of the latent images, e.g. penguin's fur skin and fish skin. The Goat case shows that the restored image is slightly damaged by even the ground truth PSF because of the bigger PSF size. In such case, the estimated PSF is not perfectly same as the ground truth. As a result, the ringing artifacts in $\hat{f}$ is more

Table 1 Experimental results of PSF candidates evaluation w.r.t. varying PSF size and λ of Eq. (10).

λ ($\times 10^{-5}$)	0	5	10	15	20	25	30	35	40	45
10×10 ∼ 20×20	176	192	191	186	179	172	160	152	142	131
20×20 ∼ 30×30	181	188	186	179	173	166	157	148	142	125
30×30 ∼ 40×40	174	179	178	176	169	165	152	147	137	127

obvious than that in $\hat{f}_{\mathrm{best}}$.

PSF candidates evaluation

Next, we evaluate the performance of the PSF candidates evaluation process Eq. (10). We synthesize 200 blurred images and 10 PSF candidates including the ground truth PSF for each image. Then, we evaluate the PSF candidates by the objective function. **Table 1** shows the number of success of 200 blurred images w.r.t. varying λ and varying PSF size. The cases $\lambda = 0$ denote that the objective function evaluates the PSF candidates with only error term. The results show that the objective function could successfully choose the ground truth PSF more than 80 percent of the trials without the regularization term. All the failure cases of $\lambda = 0$ chose the smaller size PSF than the ground truth. This result indicates that the error term can discriminate the ground truth PSF, however, the ringing artifacts caused by PSF size degrades the performance of the error term. With $\lambda = 5 \sim 15 \times 10^{-5}$, the objective function provides better results than that of $\lambda = 0$. However, the cases $\lambda > 15 \times 10^{-5}$ provide worse results according to λ. This result indicates that the regularization term assists the error term for the evaluation but relatively bigger λ makes the regularization term dominant in Eq. (10). In this experiment, the result has less correlation with PSF size. Thus, we expect that the objective function works invariant to PSF size with optimum λ value. In the latter experiments, λ is set to $5 \sim 20 \times 10^{-5}$.

Performance of entire method

Here, we validate the performance of the entire method by using 200 blurred images. PSF size is set to $10 \times 10 \sim 20 \times 20$ pixels. For each image, we compute the Peak Signal-to-Noise Ratio (PSNR) of the blurred image and the one of the restored image and compare them. The case that PSNR(f,$\hat{f}$) is greater than PSNR(f,g) represents that the restored image $\hat{f}$ is closer to the latent image f than the blurred image g. **Figure 5** plots PSNR ratio PSNR(f,$\hat{f}$)/PSNR(f,g) of the results and a red line in the figure represents the ratio equals 1. In the experiment, 159 of 200 cases result PSNR ratio greater than 1. **Figure 6** shows some of the success cases. Each caption of the blurred images and one of the restored images by estimated PSF represent PSNR(f,g) and PSNR(f,$\hat{f}$) respectively. The Mountain case is an example of higher PSNR(f,g) cases, which denotes less blurred case. Zoomed up figures show that wood area is well-recovered. Middle column shows the result of the Woman case. The restored image by estimated PSF is slightly damaged by more ringing artifacts than that by ground truth PSF, however, the detail of the image, i.e., hair and eye, are recovered. Lower PSNR(f,g) case, the Ship case, is severely blurred than other two examples. The estimated PSF is not perfectly same as the ground truth, however, the text on the ship VIKING LINE gets much better than the blurred image.

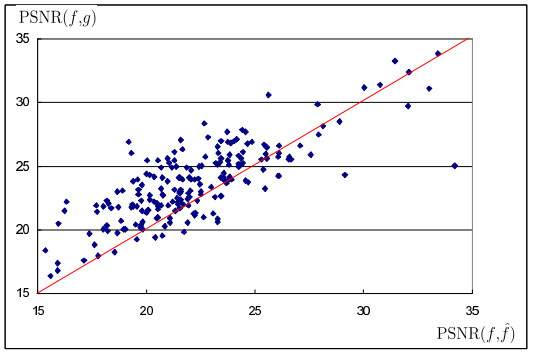

Fig. 5 Experimental results: The plots of PSNR ratio. Red line denotes PSNR ratio PSNR(f,$\hat{f}$)/PSNR(f,g) equals 1. The ratio greater than 1 indicates that the restored image $\hat{f}$ is closer to the original image f than the blurred image g.

Validation of non-uniform motion and high curvature motion

Then, we show the behavior of the proposed method when the camera motion violates our assumption that the motion is uniform speed and the motion is one direction and less curvature.

Figure 7 shows the effect of non-uniform camera speed by comparing a ULM (top) and an NULM (bottom). In **Cepstrum**, the ULM has clear line along

Fig. 6 Experimental results: Restored images of the entire method. From left to right, MOUNTAIN, WOMAN, SHIP cases are shown with NCC values between the restored images. From top to bottom, original images, blurred images, restored images by estimated PSF, restored images by ground truth PSF, and zoomed up of the restored images are shown. Red framed figures in restored images are PSFs used for deconvolution (for better visualization, we enlarge the PSFs 3 times the normal size).

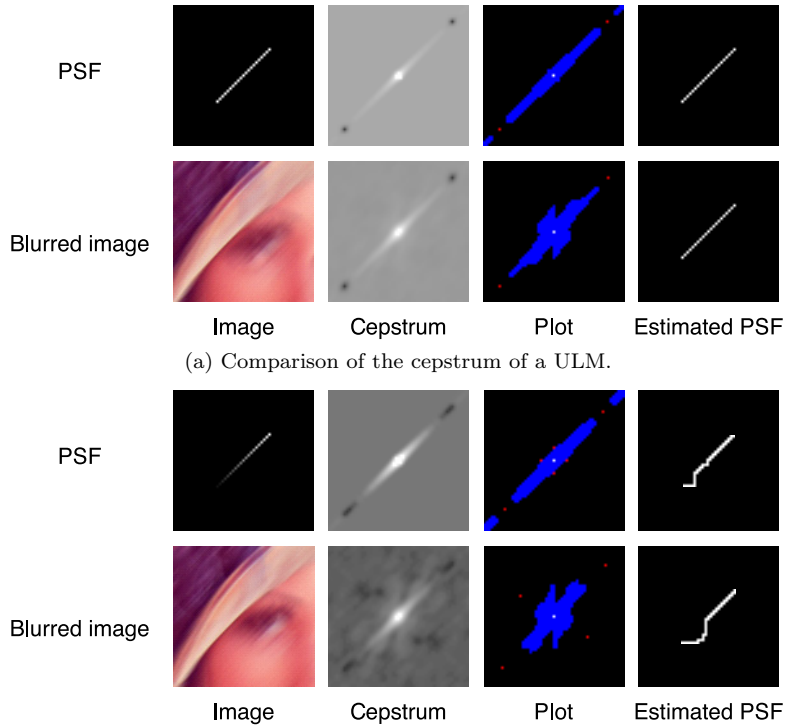

(a) Comparison of the cepstrum of a ULM.

(b) Comparison of the cepstrum of an NULM.

Fig. 7 Experimental results: PSF estimation for different motion speed: a ULM (top) and an NULM (bottom). From left to right, image, cepstrum, plotted values, and estimated PSFs are shown. In the **Plot**, the positive peak of ceptrum, negative valleys, and strong values are plotted as white, red, and blue pixels respectively.

the motion direction while the line of the NULM is less clear. **Plot** also show that strong values of the cepstrum of the NULM concentrates on the peak rather than ones of the ULM. **Estimated PSF** images show how the non-uniform camera speed affects the estimated PSF. Note that the estimated PSF by the proposed method is uniform PSF even though the correct one is non-uniform. Both the estimated PSF of the NULM are partially curved while the ones of the ULM are correct straight line. These results indicate that non-uniform motion ambiguates the strong values of the cepstrum, thus path integral based PSF estimation provides poor result.

Figure 8 shows the performance of our method for multi directional motion (**V** shape motion) and high curvature motion (**C** shape motion). For both **V** and **C** shape motions, **Cepstrum** seem to have duplicated PSF shape. However, the estimated PSF candidates are far from the correct PSF as shown in **Estimated PSF candidates**. Thus, our proposed method can not estimate multi directional

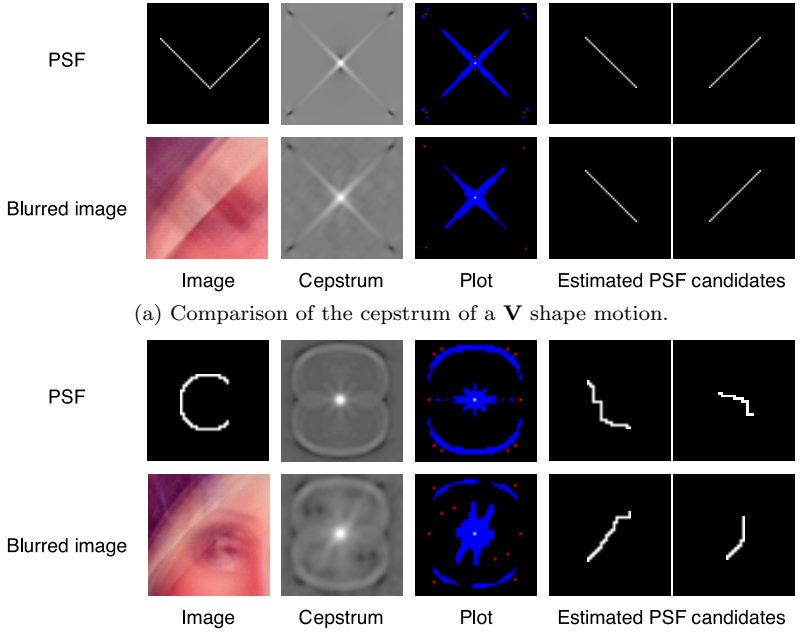

(a) Comparison of the cepstrum of a **V** shape motion.

(b) Comparison of the cepstrum of a **C** shape motion.

Fig. 8 Experimental results: PSF estimation for high curvature motion: a **V** shape motion (top) and a **C** shape motion (bottom). From left to right, image, cepstrum, plotted values, and estimated PSF candidates are shown. In the **Plot**, the positive peak of ceptrum, negative valleys, and strong values are plotted as white, red, and blue pixels respectively.

motion PSF and high curvature motion PSF.

As the above results indicate, the proposed method fails when the camera motion violates the assumption. For such motions, Bayesian approaches [4),11)] are suitable.

4.2 Real World Experiments

In the real world experiment, we compare the proposed method with a maximum likelihood algorithm Ref. 21) (Matlab's **deconvblind** function) and a Bayesian approach Ref. 11) based on variational Bayes [23)] to validate the proposed method. To deal with the noise effect on blurred images, we use a Bayesian deconvolution method [19)] as a deconvolution algorithm.

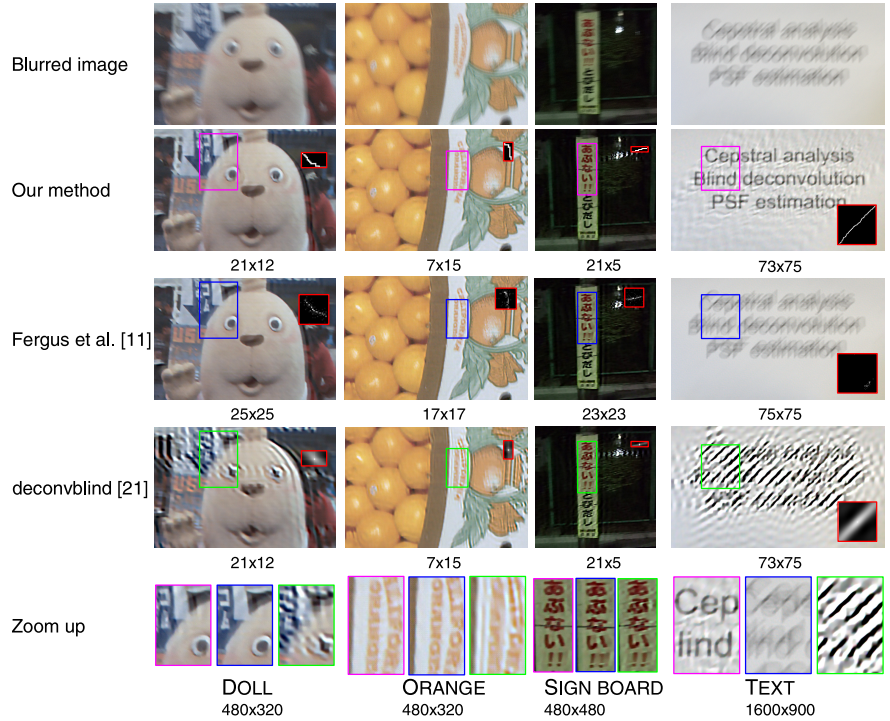

Fig. 9 Experimental results: Restored images of the real world experiment. From left to right, DOLL, ORANGE, SIGN BOARD, and TEXT scenes are shown with the image resolution. From top to bottom, blurred images, restored images by our method, restored images by Fergus, et al. [11)], restored images by deconvblind [21)], and Zoom up of restored images are shown. Red framed figures in restored images are PSFs used for deconvolution (for better visualization, we enlarge the PSFs 3 times the normal size) and each caption of restored images denotes the size of the estimated PSF. Other framed figures correspond to zoomed up regions of restored images.

Figure 9 shows the results of four scenes, DOLL, ORANGE, SIGN BOARD, and TEXT scene. The red frame in a restored image shows the estimated PSF. The caption of the restored image denotes size of the estimated PSF. The scenes DOLL and ORANGE are selected as examples of natural images. For such scenes, both our method and Ref. 11) recover clearer images, i.e., doll's eye and the text ORANGE, while Ref. 21) provides the restored images damaged by heavy ringing

artifacts. The other scenes are selected as examples of less-textured scenes: text pattern in natural scene SIGN BOARD and text-pattern only scene TEXT. For SIGN BOARD scene, both proposed method and Ref. 11) can recover satisfying quality images. The reason why Ref. 11) can recover the satisfying image is that the background area of text part in the blurred image obeys the statistics of natural images in the case of text-pattern in natural scene. Contrast to above scenes, TEXT scene has only text component in the image. For the scene, our method recovers readable text even with ringing artifacts, while Refs. 21) and 11) can not recover clearly readable images. These results indicate that our method can estimate PSFs for various scenes.

5. Conclusion

In this paper, we focus on blind deconvolution for a single blurred image taken by a standard camera undergoing a UNLM. To solve the ill-posed problem, we derive a constraint on the cepstral behavior of UNLM PSFs. Proposed method is based on the assumption that the cepstrum of a blurred image contains rough shape of the PSF. Basic idea of the proposed method is that the PSF is estimated by finding a path that maximizes path integral between the positive peak and a negative valley corresponding to the PSF in the cepstrum domain. Our method relies on dynamic programming to find these paths, yielding PSF candidates. The candidates are evaluated from the ringing artifacts appearing on the restored images. The proposed method is applied for both synthetic images and real images for validation. With synthetic images, we first assess the proposed method and then show the behavior of the proposed method when the camera motion violates the assumption on the camera motion. With real images, the proposed method is compared against other methods.

Although we limit the camera motion as uniform speed and less curvature curve, cepstral analysis can provides as satisfying results as the Bayesian approach [11] does when the camera motion follows our assumption. Moreover, the proposed method outperforms the Bayesian approach when the latent image does not obey the natural image statistics. The limitation of the proposed method caused by the assumption on the target motion was investigated in the experiments of **Validation of non-uniform motion and high curvature motion**. As we concluded, Bayesian approaches are suitable for such motions. Possible future work is to extend the cepstral approach to handle such motions. Even with such motions, their cepstra contains duplicated PSF shape as shown in Fig. 7 and Fig. 8, thus the cepstrum of a blurred image might be a clue for PSF estimation even with such motions. Further investigation like the analysis by Ding, et al. [10], which says that the spectra of some non-uniform motion have obvious features, might provide useful information for PSF estimation.

References

1) Almeida, M.S.C. and Almeida, L.B.: Blind deblurring of foreground-background images, *IEEE International Conference on Image Processing* (*ICIP*), pp.1301–1304 (2009).
2) Asai, H., Oyamada, Y., Pilet, J. and Saito, H.: Cepstral analysis based blind deconvolution for motion blur, *IEEE International Conference on Image Processing* (*ICIP*), pp.1153–1156 (2010).
3) Bhutta, A.A. and Foroosh, H.: Blind Blur Estimation Using Low Rank Approximation of Cepstrum, *International Conference on Image Analysis and Recognition* (*ICIAR*), pp.94–103 (2006).
4) Cai, J.-F., Ji, H., Liu, C. and Shen, Z.: Blind motion deblurring using multiple images, *J. Comput. Phys.*, Vol.228, No.14, pp.5057–5071 (2009).
5) Cannon, M.: Blind deconvolution of spatially invariant image blurs with phase, *IEEE Trans. Acoust., Sp., Sig. Proc.*, Vol.24, No.1, pp.58–63 (1976).
6) Chang, M.M., Tekalp, M.A. and Erdem, T.A.: Blur identification using the bispectrum, *IEEE Trans. Sig. Proc.*, Vol.39, No.10, pp.2323–2325 (1991).
7) Dai, S. and Wu, Y.: Estimating space-variant motion blur without deblurring, *IEEE International Conference on Image Processing* (*ICIP*), pp.661–664 (2008).
8) Dai, S. and Wu, Y.: Removing Partial Blur in a Single Image, *IEEE Conference on Compuer Vision and Pattern Recognition* (*CVPR*), pp.2544–2551 (2009).
9) Dijkstra, E.W.: A note on two problems in connexion with graphs, *Numerische Mathematik*, Vol.1, pp.269–271 (1959).
10) Ding, Y., McCloskey, S. and Yu, J.: Analysis of Motion Blur With a Flutter Shutter Camera for Non-linear Motion, *European Conference on Computer Vision*, pp.15–30, Springer (2010).
11) Fergus, R., Singh, B., Hertzmann, A., Roweis, S.T. and Freeman, W.T.: Removing Camera Shake From A Single Photograph, *ACM Trans. Gr.*, Vol.25, No.3, pp.787–794 (2006).
12) Gennery, D.B.: Determination of optical transfer function by inspection of frequency-domain plot, *J. Opt. Soc. Am.*, Vol.63, No.12, pp.1571–1577 (1973).
13) Ji, H. and Liu, C.: Motion Blur Identification from Image Gradients, *IEEE Con-*

ference on Computer Vision and Pattern Recognition (*CVPR*), pp.1–8 (2008).
14) Jia, J.: Single Image Motion Deblurring Using Transparency, *IEEE Conference on Computer Vision and Pattern Recognition* (*CVPR*), pp.1–8 (2007).
15) Joshi, N., Szeliski, R. and Kriegman, D.J.: PSF estimation using sharp edge prediction, *IEEE Conference on Compuer Vision and Pattern Recognition* (*CVPR*), pp.1–8 (2008).
16) Kang, X., Peng, Q., Thomas, G. and Yu, C.: Blind Image Restoration using the Cepstrum Method, *Canadian Conference on Electrical and Computer Engineering* (*CCECE*), pp.1952–1955 (2006).
17) Kundur, D. and Hatzinakos, D.: Blind image deconvolution, *IEEE Signal Processing Magazine*, Vol.13, No.3, pp.43–64 (1996).
18) Levin, A.: Blind Motion Deblurring Using Image Statistics, *Advances in Neural Information Processing Systems* (*NIPS*), pp.841–848 (2006).
19) Levin, A., Fergus, R., Durand, F. and Freeman, W.T.: Image and depth from a conventional camera with a coded aperture, *ACM Trans. Gr.*, Vol.26, pp.1–10 (2007).
20) Maki, W.F.A. and Sugimoto, S.: Blind Deconvolution Algorithm for Spatially-Invariant Motion Blurred Images based on Inverse Filtering and DST, *International Journal of Circuits, Systems and Signal Processing*, Vol.1, pp.92–100 (2007).
21) MathWorks: MatLab function deconvblind, http://www.mathworks.com/help/toolbox/images/ref/deconvblind.html
22) Mayntz, C., Aach, T. and Kunz, D.: Blur identification using a spectral inertia tensor and spectral zeros, *International Conference on Image Processing* (*ICIP*), pp.885–889 (1999).
23) Miskin, J.W.: Ensemble Learning for Independent Component Analysis, Phd, Department of Physics, University of Cambridge (2001).
24) Moghaddam, M.E. and Jamzad, M.: Motion blur identification in noisy images using mathematical models and statistical measures, *Pattern Recogn.*, Vol.40, pp.1946–1957 (2007).
25) Oliveira, J.P., Figueiredo, M.A. and Bioucas-Dias, J.M.: Blind Estimation of Motion Blur Parameters for Image Deconvolution, *3rd Iberian conference on Pattern Recognition and Image Analysis, Part II* (*IbPRIA*), pp.604–611 (2007).
26) Rom, R.: On the cepstrum of two-dimensional functions, *IEEE Trans. Inf. Theory*, Vol.21, No.2, pp.214–217 (1975).
27) Shan, Q., Jia, J. and Agarwala, A.: High-quality motion deblurring from a single image, *ACM Trans. Gr.*, Vol.27, No.3, pp.1–10 (2008).
28) Shan, Q., Xiong, W. and Jia, J.: Rotational Motion Deblurring of a Rigid Object from a Single Image, *IEEE International Conference on Computer Vision* (*ICCV*), pp.1–8 (2007).
29) Sun, H., Desvignes, M. and Yan, Y.: Motion blur adaptive identification from natural image model, *IEEE International Conference on Image Processing* (*ICIP*), pp.137–140 (2009).
30) Wiener, N.: Extrapolation, Interpolation, and Smoothing of Stationary Time Series (1949).
31) Wu, S., Lu, Z., Ong, E.P. and Lin, W.: Blind Image Blur Identification in Cepstrum Domain, *16th International Conference on Computer Communications and Networks* (*ICCCN*), pp.1166–1171 (2007).
32) Yitzhaky, Y., Mor, I., Lantzman, A. and Kopeika, N.S.: Direct method for restoration of motion-blurred images, *J. Opt. Soc. Am. A: Optics, Image Science, and Vision*, Vol.15, pp.1512–1519 (1998).

(Received November 5, 2010)
(Accepted April 12, 2011)
(Released June 24, 2011)

(Communicated by *Cha Zhang*)

Yuji Oyamada received his B.E. and M.E. degrees in Information and Computer Science from Keio University in 2006 and 2008, respectively. He is currently a Ph.D. candidate in the Graduate School of Science and Technology, Keio University. His research interests include inverse problems in both image processing and computer vision. He is a student member of the IEEE.

Haruka Asai received her M.E. degree from Keio University, Japan in 2011. She is currently working for Sony Corporation.

Hideo Saito received his B.E., M.E., and Ph.D. degrees in Electrical Engineering from Keio University, Japan, in 1987, 1989, and 1992, respectively. He has been on the faculty of Department of Electrical Engineering, Keio University, since 1992. In 1997 to 1999, he stayed in the Robotics Institute, Carnegie Mellon University as a visiting researcher. Since 2006, he has been a Professor of Department of Information and Computer Science, Keio University. He is currently the leader of the research project "Technology to Display 3D Contents into Free Space", supported by CREST, JST, Japan. His research interests include computer vision, mixed reality, virtual reality, and 3D video analysis and synthesis. He is a senior member of IEEE, and IEICE, Japan.